Journal of
Materials Chemistry B

Materials for biology and medicine

rsc.li/materials-b

ROYAL SOCIETY
OF CHEMISTRY
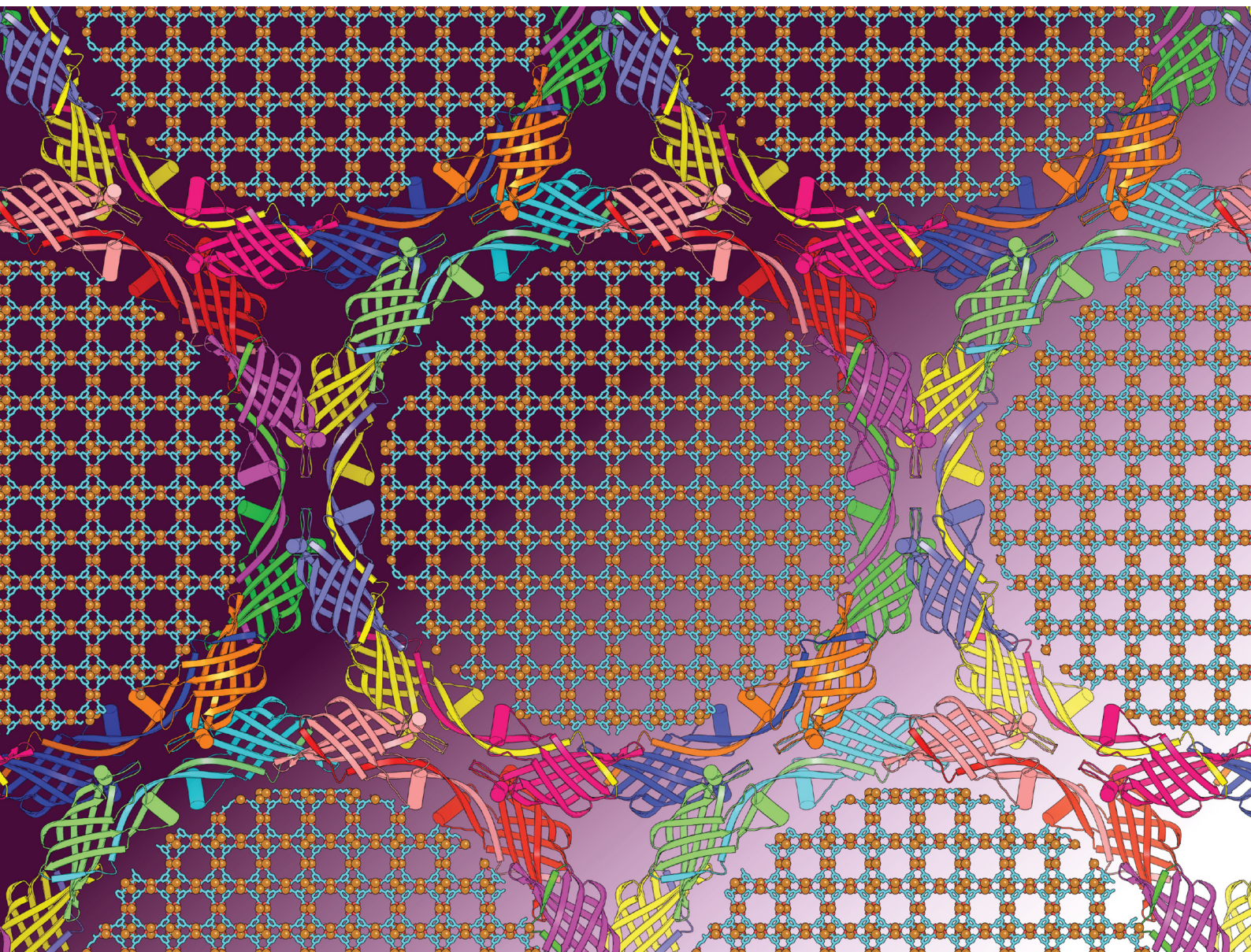
PAPER
Melissa M. Reynolds *et al.*
Deposition of metal–organic frameworks within a porous
protein crystal superstructure

Check for updates

Deposition of metal–organic frameworks within a porous protein crystal superstructure†

Jacob B. DeRoo, [iD] [b] Rojina Shrestha,‡[d] Alec Jones, [iD] [b] Deepa Rajendran,[a]
Jonathan E. Thai,[a] Robert R. Tuttle,[a] Christopher D. Snow [iD] [abc] and
Melissa M. Reynolds [iD] ★[abc]

Metal–organic frameworks (MOFs) exhibit promising catalytic properties for applications in environmental cleansing, drug delivery, and chemical warfare agent detoxification. However, their broad adoption is hindered by poor structural stability in biologically relevant (aqueous) conditions. Protein crystals, by contrast, offer exceptional environmental resilience, particularly in aqueous and intracellular environments. In this study, we developed a hybrid material combining two example MOFs (UiO-67 and CuBTC) with a porous protein crystal with an exceptionally large pore diameter (13 nm). These hybrid materials were characterized *via* single-crystal X-ray diffraction, scanning electron microscopy, transmission electron microscopy, and inductively coupled plasma atomic emission spectroscopy confirmed the successful embedding of MOFs within the protein crystal matrix. With the foundation of these hybrid materials made, expansion of this platform of materials will enable options for tackling challenging problems.

Introduction

Metal–organic frameworks (MOFs) have shown promise in a range of applications, including: petroleum-based separation,[1] additives for medical devices,[2,3] destruction of chemical warfare agents,[4,5] gas scavengers for environmental cleansing,[6,7] biosensing,[8,9] and drug delivery.[10] Although successful in some applications, the broader use of MOFs has been limited by their structural stability under use conditions, particularly in biologically relevant environments such as water, blood, PBS, and intracellular environments. On the other hand, protein crystals have remarkable stability in these environments. Thus, we set out to lay the foundation and create a material that combines both MOFs and protein crystals, leveraging the stability of both materials to create a robust protein conjugated extended framework that can serve as a platform for multiple applications, including but not limited to chemical warfare deactivation, drug delivery, and spatially efficient cascading catalytic and enzymatic pathways.

One of our motivating use cases for synthesizing new hybrid materials that embed MOF nanocrystals within a biocompatible scaffold material is the long-term potential application of eliminating chemical threats. Chemical threats (CTs) include G-class and V-class nerve agents which are especially dangerous due to their lack of color and high volatility, meaning that victims are not aware of exposure until symptoms start developing.[11–13] Exposure to these chemicals can result in skin blistering, eye and respiratory tract irritation, and asphyxiation.[14] The therapeutic window ranges from minutes to hours depending on exposure time and species. Interestingly, from an inactivation strategy, all these chemical compounds have an organophosphate bond, and degradation can be achieved *via* hydrolysis or oxidation. Of these, hydrolysis is preferred because the reaction produces safer byproducts.[15] We highlight three families of materials that can hydrolyze nerve agents: organophosphate bond cleaving enzymes such as phosphotriesterase,[16] sorbent materials like metal oxides[17] or zeolites,[18] and MOFs.[19] In the event of an emergency, rapid response with enzymes can be quite challenging with shelf life and biocompatibility. Most sorbent materials and some MOFs suffer from a similar problem: poor structure stability, low sorption capacity, few active sites, and deactivation of the active sites.[20] Even in highly porous MOFs, the majority of catalysis may occur at the surface of the crystal.[21] There is a clear need for an engineered class of materials to offer long-term stability, easy administration (proactive or reactive), high catalytic capability, and readily accessible active sites.

We also highlight not only the destructive catalytic capabilities of MOFs, but their formative capabilities as well. Previous work has shown that MOFs are capable of regenerating

[a] *Department of Chemistry, Colorado State University, 301 W. Pitkin, Chemistry Research Building, Fort Collins, Colorado, 80521, USA.*
E-mail: Melissa.Reynolds@colostate.edu
[b] *School of Biomedical Engineering, Colorado State University, USA*
[c] *Department of Chemical & Biological Engineering, Colorado State University, USA*
[d] *Cell and Molecular Biology, Colorado State University, USA*
† Electronic supplementary information (ESI) available. See DOI: https://doi.org/10.1039/d5tb00425j
‡ Deceased.

10864 | *J. Mater. Chem. B*, 2025, **13**, 10864–10870

This journal is © The Royal Society of Chemistry 2025

physiologically relevant levels of nitric oxide (NO).[2,22,23] When these MOFs are deposited on the surface of blood-contacting materials (plastic extracorporeal membrane oxygenation tubing, stents, heart valves, *etc.*), NO is regenerated from *S*-nitrosoglutathione; NO plays a critical role in preventing the aggregation of activated platelets. Activated platelet aggregation is a key step in thrombosis, causing the blood to coagulate. Typically, this is prevented by the administration of heparin; however, the systematic delivery of heparin reduces the ability of blood to clot, and suppresses both the immune and inflammatory systems.

Inspired by previous work combining MOFs with other biomacromolecules and other complex living systems,[24] where a MOF of interest is grown around non-MOF structures, we sought to create a novel hybrid MOF material with the potential for improved operational parameters relative to pure MOF. Specifically, we sought proof of concept hybrid materials wherein MOF domains, (*i.e.* nanocrystals or nanorods) are deposited inside the 13-nm diameter nanopores delimited by "CJ crystals".[25] CJ crystals are composed entirely of protein building blocks, specifically "CJ," an engineered protein variant of a putative isoprenoid binding protein (GenBank cj0420) from *Campylobacter jejuni*. After crystal growth, the porous lattice can be stabilized *via* chemical crosslinking, commonly with dialdehydes (particularly glyoxal or glutaraldehyde) or carbodiimides. While protein crystals can be catalytic (*e.g.* enzymatic crystals), the palette of canonical amino acids can limit the scope of available interactions. Indeed, many enzymes rely on coordinated metals and other prosthetic groups to achieve their intended reaction. We therefore sought to literally and figuratively combine the favorable catalytic properties of MOFs with the environmental stability and biocompatibility of another material could open the door to large-scale deployment *via* textile weaving or bioconjugation,[26] or even emergency bodily administration.[27–29] MOF encapsulation within protein crystals may provide a route to reduce immune response or other biocompatibility issue but could perhaps still preserve or amplify the catalytic activity of the guest MOF domains. While we hope the application of these materials to nerve agent hydrolysis will be realized in the future, the focus of the present contribution is instead to demonstrate the feasibility of the synthesis of a new class of material, specifically MOFs embedded into highly porous protein crystals (PPCs).

Here, we introduce a hybrid material MOF@PPC; a MOF grown in and around a porous protein crystal. While most protein crystals have significant solvent content and retain solvent channels sufficient for the internal transport of small molecules, here the term "porous" refers to crystals with pores large enough to host many MOF unit cells (*e.g.* >10 nm diameter[30]). Porous protein crystals (Fig. 1A) are a highly ordered arrangement of protein monomers that self-assemble into porous, low-density materials. One such case of a PPC is the CJ protein crystal. This protein readily forms crystals of varying, controllable size (commonly between ∼300 nm and 0.6 mm in diameter, depending on the precipitant and protein concentration), and possesses 13 nm diameter pores perpendicular to their hexagonal faces (Fig. 1B, E and F). After formation
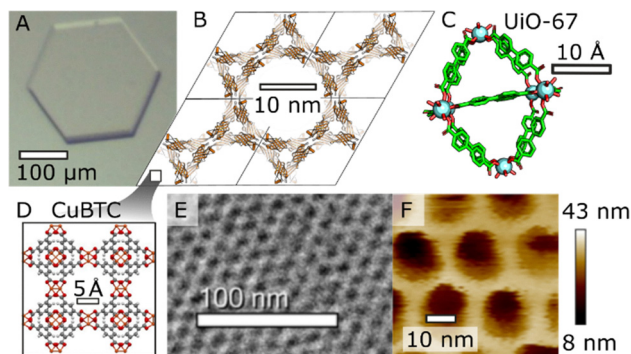

Fig. 1 Structures of the materials of interest. (A) CJ protein crystals tend to adopt a hexagonal prism habit. (B) The CJ crystal nanostructure is in the $P622$ space group and features a 13 nm diameter pore. (C) A single unit cell of the metal organic framework UiO-67 with space group $Fm\bar{3}m$. The primary pore of UiO-67 runs through the unit cell, perpendicular to the page. (D) 4 unit cells of CuBTC, arranged in a 2 × 2 pattern, with space group $Fm\bar{3}m$. The pore of CuBTC runs through the union of 4 CuBTC unit cells. (E) TEM of a stained microtome slice of a CJ crystal interior, highlighting the periodicity of the pores. (F) AFM of the CJ protein crystal's surface, highlighting the porosity of the material.

CJ crystals can be crosslinked, becoming extremely tough and capable of withstanding diverse environments and stresses, such as in pure water, high salt conditions, the presence of cells,[27] and ingestion by mosquitoes.[29] CJ crystals have also been explored for guest molecule installation and delivery.[29] CJ monomers first form a domain-swapped dimer and then proceed to assemble into a $P622$ lattice reminiscent of a honeycomb. The protein components delimit a tightly spaced hexagonal array of nanopores, one 13 nm pore repeating every 18 nm[31] (Fig. 1E and F). We hypothesize that nanoscale MOF domains deposited inside CJ crystals may feature a large accessible surface area, and thus improved transport to MOF active sites and improved catalytic performance over freestanding monolithic MOF microcrystals.[22,32] Prior, it was unclear if the solution conditions needed for MOF growth (typically harsh organic solvents and high temperatures) would be compatible with host protein crystals. Because of the remarkable stability of crosslinked CJ crystals, we proceeded to test their capability to withstand the harsh organic solvents required to grow both CuBTC and UiO-67. We hypothesized that the CJ crystal's high porosity and large solvent channels would permit the nucleation and growth of MOF nanocrystals that span multiple unit cells.

The MOF CuBTC (aka HKUST-1, MOF-199) is a well characterized MOF for which there are robust synthetic procedures known.[33,34] CuBTC is composed of copper(II) centers and benzene-1,3,5-tricarboxylate linker molecules (aka trimesic acid) and readily grows on many surfaces,[2] making it a top candidate for proof of concept studies. CuBTC has been applied in carbon dioxide gas storage,[7] catalytic breakdown of 2-CEES/HD,[5] and more. CuBTC is a MOF whose unique building unit is composed of two copper atoms, held together by four BTC molecules in a pinwheel shape. The CuBTC unit cell has a side length of approximately 2.6 nm, therefore it would be theoretically possible to fit 5 copies of the unit cell in the pore of the

CJ crystal linearly across the diameter (Fig. 1D). The catalytic capabilities of CuBTC to degrade G-class nerve agents are less favorable, especially when compared to UiO-67.[19] UiO-67 is a newer MOF than CuBTC and has found applications in gas storage,[35] chemical warfare agent detoxification,[4] bioimaging,[36,37] and more. Its structure is composed of ZrO clusters and biphenyl-4,4′-dicarboxylic acid linkers.

To the best of our knowledge, this is the first report of the creation of a MOF@PPC semi-biological material. While the catalytic deactivation of CTs is a long-term application, this paper reports only the preparation, characterization and stability of the CuBTC@CJ and UiO-67@CJ.

Results

CuBTC grows mostly in the pores of the protein

After exposure to CuBTC growth conditions, host CJ crystals underwent a color transformation from a pale yellow to brilliant blue (Fig. 2A and B). As assessed in physical manipulation of such crystals under a stereozoom microscope, the blue color appeared to be uniform throughout the crystal interior. We also observed green crystals after CuBTC@CJ formation (Fig. S1, ESI†). To ensure that the CuBTC MOF had indeed grown in and around the CuBTC@CJ crystals, single crystal X-ray diffraction (scXRD) and scanning electron microscope (SEM) data were collected. SEM images of the surface show sparse, individual CuBTC crystals deposited into surface imperfections of the protein crystal (Fig. 3A and C). scXRD data show full and intact Debye–Scherrer rings (Fig. S2, ESI†) that can be converted to a pXRD "fingerprint" (Fig. 4A and C). This implies that the X-ray beam (∼ 8 μm diameter for ALS beamline 4.2.2), while passing through the host CJ crystal, was also passing through MOF domains in all orientations. Notably, the XRD intensity did vary with goniometer angle (angle between crystal face and X-ray source), consistent with the variable pathlength of the host crystal (Fig. S3, ESI†). This scXRD data is consistent with a significant portion of the CuBTC having grown within the pores of the CJ crystal. In contrast, a large single CuBTC crystal would generate a single set of Bragg reflections. For comparison, we pressed a pure CuBTC powder into a 10 μm crystal loop (Fig. S4A, ESI†), where individual CuBTC crystals clung to the loop. We obtained a diffraction pattern that is intermediate between the single lattice Bragg peaks and the powder diffraction Debye–Scherrer rings (Fig. S4B, ESI†). Notably, the presence
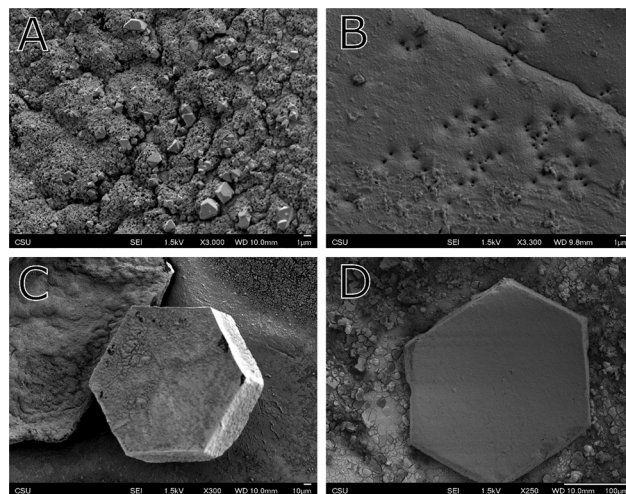

Fig. 3 SEM images of CuBTC@CJ and UiO-67@CJ. (A) SEM of the surface of a CuBTC@CJ crystal at 3000× magnification. Individual micro CuBTC crystals are observable with their expected octahedral habit. (B) SEM of the surface of a UiO-67@CJ crystal at 3000× magnification. Instead of the expected octahedral morphology of UiO-67, a "blanket" is observed. (C) The surface of a CuBTC@CJ crystal at 300× magnification. (D) The surface of a UiO-67@CJ crystal at 300× magnification.
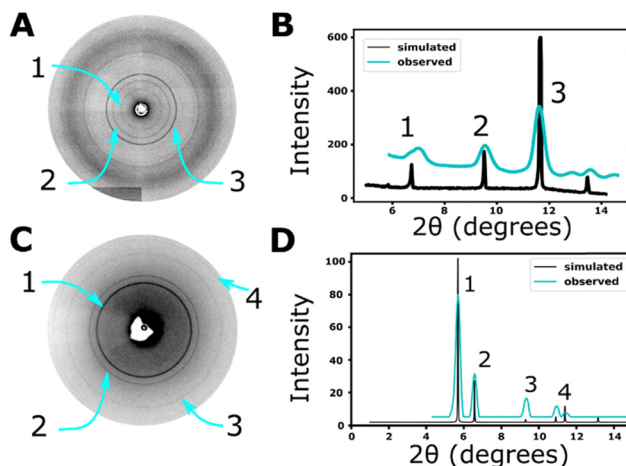

Fig. 4 Single crystal X-ray diffraction (collected on the ALS 4.2.2 beamline) patterns and Debye−Scherrer rings of (A) CuBTC@CJ and (C) UiO-67@CJ, respectively. Extracted powder X-ray diffraction patterns from the scXRD, overlaid with the simulated PXRD patterns of (B) CuBTC and (D) UiO-67, respectively.

of CuBTC nanocrystals within the interior of the CJ crystal does not preclude the formation of CuBTC nano- and microcrystals adhered to the CJ crystal surface. Indeed, SEM imaging clearly reveals surface associated CuBTC microcrystals (Fig. 3A).

To further demonstrate that the MOF was growing throughout the protein crystals' interior, the CuBTC was leached out of the CJ crystal by soaking in 10 μL water for 24 hours. The supernatant was analyzed for copper concentration via inductively coupled plasma atomic emission spectroscopy (ICP-AES) by Huffman Hazen Labs (Golden, CO). The copper content in
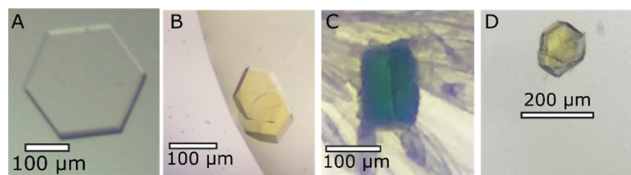

Fig. 2 The various colors of CJ crystals after being loaded with different MOFs. (A) An empty CJ crystal. (B) An empty CJ crystal that has recently been crosslinked with glyoxal. (C) A crosslinked CJ crystal with CuBTC grown in and around the crystal. (D) A crosslinked CJ crystal with UiO-67 grown in and around the crystal.

10866 | J. Mater. Chem. B, 2025, 13, 10864–10870

This journal is © The Royal Society of Chemistry 2025

the supernatant would have been sufficient to fill 74% of the crystal's interior with CuBTC (Fig. S5, ESI†). After 24 hours, the crystals had lost much of their visible color and had not changed in size significantly before and after CuBTC growth (Fig. S6, ESI†).

We performed azimuthal integration (see **https://github. com/jbderoo/MOF_in_CJ** for extensive explanation and demonstration) on the scXRD data to generate pXRD data (Fig. 4A and B) and compared it to the expected pXRD pattern of CuBTC (computed with the structure of CuBTC and VESTA). While CJ crystals maintain macroscopic stability and overall shape in organic solvents like DMSO, the precise nanostructure is lost. No high-resolution Bragg reflections were detected in the scXRD from the protein crystal. In contrast, the MOF pXRD "fingerprint", particularly peaks (2,0,0), (2,2,0), and (2,2,2), were extremely similar with peak angular displacement difference of less than 1%. This indicates that the CuBTC metal organic framework is present. From the computed pXRD curve, the Debye–Scherrer equation (eqn (1)) can be used to approximate the size of the polycrystalline material present (D), from the dimensionless shape factor (K, assumed to be 0.9), X-ray wavelength ($\lambda = 0.107$ nm), the full width half max value ($\beta = 0.273°$), and the Bragg angle ($\theta = 11.65$). The reported instrument (Advanced Light Source synchrotron) peak broadening of 9.7 μrad would therefore contribute $<0.4\%$ of the measured β. Applying the equation yields an approximate nanocrystal size of 20.7 nm; $\sim 60\%$ larger than the nominal 13 nm diameter of the CJ crystal pore. While part of this moderate discrepancy may be due to the approximate nature of the calculation, it is also likely that nanocrystals confined within the host protein crystal nanopores could have anisotropic shape. For example, cylindrical nanorods with diameter of 13 nm and height of 35 nm (~ 7 CJ crystal unit cells) would have approximately the same volume as spheres with diameter 20.7 nm. A somewhat longer nanorod length (48 nm) results if we correct the shape factor K to 1.0 for rod-shaped crystallites[38] (*via* the larger predicted $D = 23$ nm). Larger contributing nanocrystals could also be found at crystal defect sites and the crystal surface, though the most visible surface crystals in Fig. 3A are much larger.

$$D = \frac{K\lambda}{\beta \cos\theta} \tag{1}$$

While most CuBTC growth conditions rely on high temperature, here we are growing CuBTC inside and outside the host CJ crystals at room temperature (298 K). Surface exposed acidic amino acids (namely aspartic acid and glutamic acid) within the CJ nanopores could bind Cu atoms, thus favoring CuBTC nucleation and growth within the pores. In this model for nucleation, several BTC molecules will come and bind to a copper-histidine complex, followed by more coppers onto the recently bound BTC molecules, and the process repeats. A possibly over-simple model for MOF growth would be to assume uniform deposition of MOF nanocrystals throughout the body of host CJ crystals. In this case, varying the crystal orientation *via* the goniometer would change the number of MOF unit cells intercepted by the X-ray beam proportional to the path length of the host CJ crystal, thereby resulting in angle dependence of the total pXRD diffraction intensity (Fig. S2, ESI†).

The porous protein crystal can host different MOFs: UiO-67 was grown in/outside of the CJ crystal, demonstrating the ability to grow a variety of MOFs in conjunction with the CJ crystal

Crosslinked CJ crystals were rested in a UiO-67 precursor solution inspired by UiO-67 synthesis procedures[39,40] for 24 hours. A subtle color change of pale yellow to opaque yellow/white (Fig. 2C) was observed. SEM images of the UiO-67@CJ crystals did not reveal individual crystals of UiO-67 latched onto the surface of the CJ crystals, but instead showed a smooth "blanket" on the surface of the SEM (Fig. 3B and D). Critically, these crystals produced continuous Debye–Scherrer rings (Fig. 4C). After azimuthal integration, the observed pXRD pattern was again a close match to the expected pattern (Fig. 4D), specifically comparing peaks with Miller indices (1,1,1), (2,0,0), (2,2,0), and (3,1,1). The observed diffraction pattern and subtle color change were consistent with the growth of UiO-67 in and around the CJ protein crystal.

The metal organic frameworks could be used as a capping or protecting agent for guests installed into the protein crystal

Given the limited resolution of the SEM images, it was not possible to directly observe the presence or absence of open nanopores from the original crystal. Therefore, to provide supporting evidence for the supposition that UiO-67 growth sealed the CJ nanopore array, we turned to confocal microscopy. Confocal microscopy allows us to image a Z-stack with focal planes inside large CJ crystals. We can incubate such crystals in a volume of fluorescent protein after UiO-67 growth, and observe the change in fluorescence of the UiO-67@CJ crystals.

After observing the change in fluorescence of some UiO-67@CJ protein crystals, we found that UiO-67@CJ crystals nearly completely blocked the entry of super folder GFP (sfGFP) from entering the crystal interior (Fig. 5A). Initial values of fluorescence are taken as the zero point. After 60 seconds an additional 1 μL drop of super folder GFP (sfGFP) (0.4 mg mL^{-1} sfGFP in 50 mM pH 7.4, 10% glycerol) was added to create a strong driving force for sfGFP uptake. The resulting sfGFP transport caused a gradual increase in background fluorescence. The crystal that underwent UiO-67 growth remained significantly darker than the sister crystal that was incubated in water for an equal amount of time (30 minutes) (Fig. 5B and C). Time-lapse z-stack photos are available in Fig. S7 (ESI†), along with a loading time lapse video of the system (and a sped-up gif) at our github.

To add another line of evidence in support of CuBTC growth throughout the CJ crystal interior, we took time resolved confocal microscopy images of the CJ crystals during incubation in a CuBTC growth solution. While monitoring the interior of the crystal (median z-stack values) over the course of an hour, we observed large changes throughout the CJ crystal interior. Specifically, by monitoring the fluorescence emission ratio (excitation at 488 nm relative to excitation at 405 nm) we could see a sizable increase in green fluorescence relative to blue
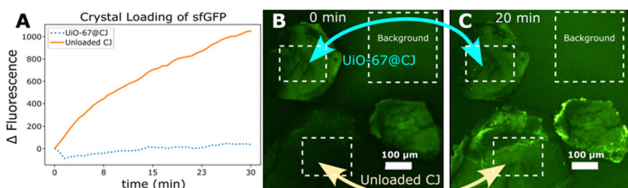
Fig. 5 (A) Change in fluorescence over time for 2 crystals and the background. 2 crystals are monitored for their change in fluorescence (accumulation of sfGFP, ROI highlighted with white dotted boxes) over time. (B) A confocal image of the crystals (both UiO-67 loaded and not) as soon as the sfGFP is added. ROI's are shown in white dotted boxes for each region, corresponding to the labels in panel (A). (C) The same crystals 20 minutes later, allowing sufficient time for sfGFP to diffuse into the pores of the CJ crystals.

fluorescence. Videos and stills of this process are supplied in Fig. S8 (ESI†).

Materials & methods

CuBTC synthesis

Cu(NO$_3$)$_2$ × 2.5 H$_2$O (copper(II) nitrate hemipentahydrate) and BTC (benzene-1,3,5 tricarboxylic acid) were purchased from Sigma Aldrich and used without further purification. 2.45 g Cu(NO$_3$)$_2$ and 1.16 g BTC were sonicated into pure 10 mL DMSO (dimethyl sulfoxide)[33] to form a stable precursor solution of CuBTC. Vortexing and sonication were used until dissolution was complete.

UiO-67 synthesis

ZrCl$_4$ (zirconium tetrachloride) and BPDC (biphenyl-4,4′-dicarboxylate) were purchased from Sigma Aldrich and used without any further purification. A 1 mL sample of DMF (n,n-dimethyl formamide) was prepared with the ZrCl$_4$ and the BPDC linker at 1:1 stoichiometry at 17 mM. 5 µL water was added to the solution. The solution was vortexed and sonicated until complete dissolution was reached.[39,40]

Protein expression & purification

As detailed by Huber et al., a gene encoding "CJ" an optimized variant of GenBank ID CJ0420 cloned into the pSB3 expression vector.[25] This was expressed in BL21 E. coli. The target protein was purified via metal affinity chromatography column.[41]

CJ porous protein crystal fabrication and crosslinking

The aforementioned protein was crystalized via sitting drop vapor diffusion by mixing 1 µL of 14 mg mL^{-1} purified protein with 1 µL of crystallization buffer (3.2 M ammonium sulfate, pH 6.5, 0.1 M bis-tris buffer). Smaller crystals (<10 µm in diameter) were synthesized using a batch crystallization method. Briefly, 1 volume of concentrated CJ (~40 mg mL^{-1}) was combined with 5 volumes of precipitant buffer (3.5 M ammonium sulfate, pH 7.0, 0.1 M bis-tris), and incubated at room temperature. Crystals in both cases formed over the course of 3–7 days. After sizeable crystals had formed (100–150 µm diameter) they were washed three times in 4.2 M TMAO (trimethylamine oxide) at pH = 7.5 for 10 minutes per wash.

The crystals were then crosslinked for 2 hours in the TMAO solution with 1% glyoxal and 50 mM DMAB. These conditions were previously optimized to ensure complete crosslinking and crystal integrity.[25] For the microcrystals used in the confocal fluorescence experiments, fluorescent labelling of the crystals was achieved by addition of NHS-Pacific blue (Invitrogen™, # P10163), to a final concentration of 2 mM during the crosslinking step.

MOF@CJ combination

The crosslinked protein crystals were submerged in the respective MOF precursor solutions for 24 hours at room temperature, into a Corning Pyrex 9 depression glass spot plate. They were then transferred to a clean solution of their respective organic solvents and given a gentle swirl to knock off any loosely adhered surface MOF that had grown on the surface of the crystal. These crystals are the final result, and are named CuBTC@CJ and UiO-67@CJ crystals, respectively.
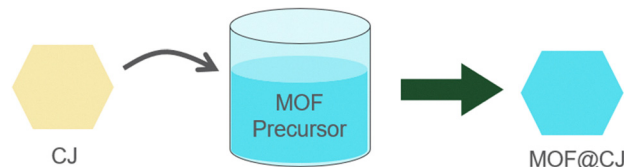
MOF@CJ material analysis

Putative CuBTC@CJ single crystals were shot on a single crystal X-ray diffractometer (scXRD). Data were collected at either the Advanced Light Source (ALS) Beamline 4.2.2 at Berkeley National Laboratory, or on a local Rigaku HomeLab. When a polycrystalline material is shot on an scXRD, the resulting diffraction patterns contain Debye–Scherrer rings instead of individual Braggs spots. scXRD data can be converted to powder X-ray diffraction data (pXRD) data by azimuthal integration (averaging the radial intensity). Examining the meta data of the scXRD image provides a conversion of pixels to radial distance, as well as the sample to detector distance. Using eqn (1), meta data from the image, and the pixel intensity vs. radial distance data, we compute pXRD data from scXRD for direct comparison (Fig. S2, ESI†). Example processing scripts are available at our github. The crystal lattice of the CJ crystal is disrupted by the organic solvents, and so its Braggs spots are lost. Eqn (2) (Bragg's law) relates the diffraction angle (2θ) to the radial distance (r) and the distance between the sample and the detector (D).

$$2\theta = \tan^{-1}\left(\frac{r}{D}\right) \tag{2}$$

SEM images of MOF@CJ crystals

Crystals were made following the MOF@CJ combination protocol previously described. Afterwards, the crystals were gently cleaned in their respective growth solvent (DMF/DMSO). SEM imaging was performed using a JEOL JSM-6500F microscope. An accelerating voltage of 15.0 kV was used to image the MOF@CJ crystals. All samples were prepared by looping them

10868 | J. Mater. Chem. B, 2025, **13**, 10864–10870

This journal is © The Royal Society of Chemistry 2025

from cleansing media onto an aluminum SEM stage into 2 µL of DI water. The samples were allowed to dry overnight before they were placed under vacuum and coated with 20 nm of gold prior to imaging.

Confocal fluorescence microscopy of MOF@CJ crystals

Both UiO-67@CJ crystals and control CJ crystals were imaged side by side using confocal fluorescence microscopy, with 488 nm laser excitation and a 530 nm long-pass filter (as well as a 405 laser excitation with a 450–470 bandpass filter for Pacific blue-stained crystals). During imaging, polyhistidine-tagged, monomeric sfGFP was added (0.4 µg total), and both crystals were imaged over a 30-minute period. Changes in relative fluorescence were compared between wild-type and MOF@CJ crystals. All images were obtained using a Nikon TE2000-U inverted microscope spinning disk confocal microscope. Image analysis was performed in Nikon NIS Elements, version 5.21.00 (Build 1483).

Conclusions and future work

Notably, the CJ crystals used in this work were relatively large (approximately 100 µm in diameter and 2 µg) crosslinked protein crystals, produced via sitting drop vapor diffusion. After 72 h of growth, crystals were individually and manually processed via looping, cleaning, crosslinking, and transfer to MOF growth conditions. The current reliance on manual processing prevents scaled up production of milligram scale quantities of MOF@CJ and the application of assays that require more than a few micrograms of material (e.g. gas adsorption porosity measurements or catalysis quantification). Therefore, future work will be required to adapt the material production methods to CJ crystals produced via scalable batch crystallization methods. While batch crystallization of CJ is routine, the product most often tends to be large quantities of microcrystals (e.g. with ~10 µm diameter). Additional process optimizations will be needed for the batch growth of larger CJ crystals as well as careful tuning to minimize freestanding MOF crystal growth. Fig. S9 (ESI†) demonstrates the use of confocal microscopy to localize several CJ microcrystals among a large collection of CuBTC microcrystals, thereby illustrating the potential challenge of separating MOF@CJ microcrystals from surrounding standard MOF microcrystals. Fig. S10 (ESI†) highlights potential UiO-67 nanocrystals on CJ microcrystals via SEM. Given future milligram quantities of larger CJ crystals, it may be possible to separate these from MOF overgrowth via size selection methods.

In summary, we present a new combination of materials with a protein crystal acting as a scaffold for internal and surface growth of metal organic frameworks. Both protein crystals and MOFs have their own expansive history and use cases, and this paper marks the first reported combination of these porous materials. The MOF@PPC combination has the potential to support highly organized, spatially optimized chemical reactions. Candidate application for the semi-biological materials include hyper stabilization, dual catalysis, gas storage, separation, delivery, and protective guest delivery. Future work includes exploring unique doping combinations, finding greener and more protein friendly MOF deposition conditions, and material synthesis scaleup. Comparing the relative catalytic activity of solution-suspended versus protein-encapsulated MOFs will be particularly interesting. Hypothetically, the high surface area and lattice defect density expected for MOF nanocrystals grown within protein crystals could enhance catalytic applications thereof.

Author contributions

J. D. was responsible for conceptualization, investigation, formal analysis, software, writing – original draft, and writing – review & editing. S. R. was responsible for investigation. A. J. was responsible for conceptualization, investigation, writing – review & editing. D. R. was responsible for investigation. J. T. was responsible for investigation and writing – reviewing & editing. R. T. was responsible for writing – reviewing & editing. C. S. was responsible for project administration, methodology, conceptualization, funding acquisition, and writing – reviewing & editing. M. R. was responsible for project administration, methodology, conceptualization, funding acquisition, and writing – reviewing & editing.

Conflicts of interest

The authors have no conflicts to declare.

Data availability

The code (python files) and data (.img files) for this publication can be found at **https://github.com/jbderoo/MOF_in_CJ**. The code is up to date, and is the exact version of what was used to do the analysis.

Acknowledgements

Notes and references

1 X. Zhang, X. Wang, F. Gao, Y. Chen, H. Liu, P. Zhou, Z. Kang, Y. Wang and W. Fan, *Mater. Adv.*, 2024, **5**, 3135–3157.

2 M. J. Neufeld, J. L. Harding and M. M. Reynolds, *ACS Appl. Mater. Interfaces*, 2015, **7**, 26742–26750.

This journal is © The Royal Society of Chemistry 2025

J. Mater. Chem. B, 2025, **13**, 10864–10870 | **10869**

3 Y. Zang, T. R. Roberts, A. I. Batchinsky and M. M. Reynolds, *ACS Appl. Bio Mater.*, 2020, **3**, 3535–3543.

4 J. Zhao, D. T. Lee, R. W. Yaga, M. G. Hall, H. F. Barton, I. R. Woodward, C. J. Oldham, H. J. Walls, G. W. Peterson and G. N. Parsons, *Angew. Chem., Int. Ed.*, 2016, **55**, 13224–13228.

5 A. Roy, A. K. Srivastava, B. Singh, T. H. Mahato, D. Shah and A. K. Halve, *Microporous Mesoporous Mater.*, 2012, **162**, 207–212.

6 L. Grajciar, A. D. Wiersum, P. L. Llewellyn, J.-S. Chang and P. Nachtigall, *J. Phys. Chem. C*, 2011, **115**, 17925–17933.

7 H. W. B. Teo, A. Chakraborty and S. Kayal, *Appl. Therm. Eng.*, 2017, **110**, 891–900.

8 S. Kulandaivel, H.-T. Chen, C.-H. Lin and Y.-C. Yeh, *J. Mater. Chem. B*, 2023, **11**, 10362–10368.

9 D. Luo, J. Huang, Y. Jian, A. Singh, A. Kumar, J. Liu, Y. Pan and Q. Ouyang, *J. Mater. Chem. B*, 2023, **11**, 6802–6822.

10 E. Binaeian, H. Nabipour, S. Ahmadi and S. Rohani, *J. Mater. Chem. B*, 2023, **11**, 11426–11459.

11 R. D. Gupta, M. Goldsmith, Y. Ashani, Y. Simo, G. Mullokandov, H. Bar, M. Ben-David, H. Leader, R. Margalit, I. Silman, J. L. Sussman and D. S. Tawfik, *Nat. Chem. Biol.*, 2011, **7**, 120–125.

12 S. Mukherjee and R. D. Gupta, *J. Toxicol.*, 2020, 3007984.

13 L. G. Costa, *Toxicol. Sci.*, 2018, **162**, 24–35.

14 CDC, ToxFAQs for Nerve Agents (GA, GB, GD, VX), https://wwwn.cdc.gov/TSP/ToxFAQs/ToxFAQsDetails.aspx?faqid=524&toxid=93.

15 G. W. Peterson and G. W. Wagner, *J. Porous Mater.*, 2014, **21**, 121–126.

16 A. N. Bigley and F. M. Raushel, *Chem. – Biol. Interact.*, 2019, **308**, 80–88.

17 G. W. Wagner, G. W. Peterson and J. J. Mahle, *Ind. Eng. Chem. Res.*, 2012, **51**, 3598–3603.

18 Q. Meng, D. C. Doetschman, A. K. Rizos, M. H. Lee, J. T. Schulte, A. Spyros and C. W. Kanyi, *Environ. Sci. Technol.*, 2011, **45**, 3000–3005.

19 K. Vellingiri, L. Philip and K.-H. Kim, *Coord. Chem. Rev.*, 2017, **353**, 159–179.

20 J. E. Mondloch, M. J. Katz, W. C. Isley, P. Ghosh, P. Liao, W. Bury, G. W. Wagner, M. G. Hall, J. B. Decoste, G. W. Peterson, R. Q. Snurr, C. J. Cramer, J. T. Hupp and O. K. Farha, *Nat. Mater.*, 2015, **14**, 512–516.

21 R. R. Tuttle, R. G. Finke and M. M. Reynolds, *ACS Catal.*, 2022, **12**, 8055–8068.

22 A. C. Melvin, R. R. Tuttle, M. Mohnike and M. M. Reynolds, *ACS Mater. Lett.*, 2022, **4**, 2434–2439.

23 J. L. Harding and M. M. Reynolds, *J. Mater. Chem. B*, 2014, **2**, 2530–2536.

24 R. Riccò, W. Liang, S. Li, J. J. Gassensmith, F. Caruso, C. Doonan and P. Falcaro, *ACS Nano*, 2018, **12**, 13–23.

25 T. R. Huber, L. F. Hartje, E. C. McPherson, A. E. Kowalski and C. D. Snow, *Small*, 2017, **13**, 1602703.

26 L. F. Hartje, D. A. Andales, L. P. Gintner, L. B. Johnson, Y. V. Li and C. D. Snow, *Crystals*, 2023, **13**(2), 352.

27 L. F. Hartje, H. T. Bui, D. A. Andales, S. P. James, T. R. Huber and C. D. Snow, *ACS Biomater. Sci. Eng.*, 2018, **4**, 826–831.

28 J. D. Stuart, D. A. Hartman, L. I. Gray, A. A. Jones, N. R. Wickenkamp, C. Hirt, A. Safira, A. R. Regas, T. M. Kondash, M. L. Yates, S. Driga, C. D. Snow and R. C. Kading, *PNAS Nexus*, 2022, **1**, pgac190.

29 J. D. Stuart, N. R. Wickenkamp, K. A. Davis, C. Meyer, R. C. Kading and C. D. Snow, *Int. J. Mol. Sci.*, 2023, **24**(3), 2549.

30 A. A. Jones and C. D. Snow, *Chem. Commun.*, 2024, **60**(45), 5790–5803.

31 D. Wang, J. D. Stuart, A. A. Jones, C. D. Snow and M. J. Kipper, *Nanoscale*, 2021, **13**, 10871–10881.

32 V. Mouarrawis, R. Plessius, J. Ivar van der Vlugt and J. N. H. Reek, *Front. Chem.*, 2018, **6**, 623.

33 H. V. Doan, Y. Fang, B. Yao, Z. Dong, T. J. White, A. Sartbaeva, U. Hintermair and V. P. Ting, *ACS Sustainable Chem. Eng.*, 2017, **5**(9), 7887–7893.

34 J. Kim, H. Y. Cho and W. S. Ahn, *Catal. Surv. Asia*, 2012, **16**, 106–119.

35 S. Chavan, J. G. Vitillo, D. Gianolio, O. Zavorotynska, B. Civalleri, S. Jakobsen, M. H. Nilsen, L. Valenzano, C. Lamberti, K. P. Lillerud and S. Bordiga, *Phys. Chem. Chem. Phys.*, 2012, **14**, 1614–1626.

36 R. Chen, J. Zhang, J. Chelora, Y. Xiong, S. V. Kershaw, K. F. Li, P. K. Lo, K. W. Cheah, A. L. Rogach, J. A. Zapien and C. S. Lee, *ACS Appl. Mater. Interfaces*, 2017, **9**, 5699–5708.

37 Y. A. Li, C. W. Zhao, N. X. Zhu, Q. K. Liu, G. J. Chen, J. B. Liu, X. D. Zhao, J. P. Ma, S. Zhang and Y. Bin Dong, *Chem. Commun.*, 2015, **51**, 17672–17675.

38 D.-M. Smilgies, *J. Appl. Crystallogr.*, 2009, **42**, 1030–1034.

39 G. Kaur, S. Øien-ØDegaard, A. Lazzarini, S. M. Chavan, S. Bordiga, K. P. Lillerud and U. Olsbye, *Cryst. Growth Des.*, 2019, **19**, 4246–4251.

40 M. J. Katz, Z. J. Brown, Y. J. Colón, P. W. Siu, K. A. Scheidt, R. Q. Snurr, J. T. Hupp and O. K. Farha, *Chem. Commun.*, 2013, **49**, 9449–9451.

41 A. E. Kowalski, L. B. Johnson, H. K. Dierl, S. Park, T. R. Huber and C. D. Snow, *Biomater. Sci.*, 2019, **7**, 1898–1904.

10870 | *J. Mater. Chem. B*, 2025, **13**, 10864–10870

This journal is © The Royal Society of Chemistry 2025